



# Comparison of photocatalytic reaction-induced selective corrosion with photocorrosion: Impact on morphology and stability of Ag-ZnO



Xinlong Ma<sup>a,b</sup>, Hao Li<sup>a,b</sup>, Tongyao Liu<sup>a,b</sup>, Shanshan Du<sup>a,b</sup>, Qinqing Qiang<sup>a,b</sup>,  
Yuhua Wang<sup>a,b,\*</sup>, Shu Yin<sup>c</sup>, Tsugio Sato<sup>c</sup>

<sup>a</sup> Key Laboratory for Special Function Materials and Structure Design of the Ministry of Education, Lanzhou University, Lanzhou 730000, PR China

<sup>b</sup> Department of Materials Science, School of Physical Science and Technology, Lanzhou University, Lanzhou, 730000, PR China

<sup>c</sup> Institute of Multidisciplinary Research for Advanced Materials, Tohoku University, 2-1-1 Katahira, Aoba-ku, Sendai 980-8577, Japan

## ARTICLE INFO

### Article history:

Received 2 July 2016

Received in revised form 7 August 2016

Accepted 14 August 2016

Available online 16 August 2016

### Keywords:

Ag-ZnO

Photocorrosion

Selective corrosion

Photocatalytic stability

## ABSTRACT

In previous work, the photocatalytic stability during the recycled degradation is employed to evaluate the inhibitory effect of photocorrosion. Then, a significant question arises: is the photocatalytic stability only related to the photocorrosion for zinc oxide (ZnO)? The answer turns out to be no in our work. The phenomenon of photocatalytic reaction-induced selective corrosion of ZnO nanosheets was firstly revealed. It is found that the special corrosion not only needs ultraviolet (UV) light irradiation, but also results from the photocatalytic reaction. Then, the impacts of this special corrosion and photocorrosion on morphology and photocatalytic stability were compared. It is found that the photocatalytic reaction-induced selective corrosion shows more mass loss, more selective etching and more decrease of unit mass photocatalytic activity than that of photocorrosion. The results indicate that the special corrosion-induced active face loss rather than the photocorrosion-induced mass loss can be fatal for the photocatalytic stability. Accordingly, a direct and visual confirmation of inhibitory effect of loaded Ag against selective corrosion is revealed.

© 2016 Elsevier B.V. All rights reserved.

## 1. Introduction

It is well known that semiconductor-based photocatalysts have received great attention as efficient, stable, and environmentally friendly materials in the field of environmental protection issues [1–7]. ZnO is one of the most renowned photocatalysts among various semiconductors with a wide band-gap of 3.37 eV and a large exciton binding energy of 60 meV [8]. The photocatalytic properties of ZnO are strongly dependent on its structures, including the morphology, aspect ratio, size, and orientation of crystal [9–18].

Among these exploration of ZnO crystals, for one thing, it is highly confirmed that the photocatalytic activity of ZnO is strongly dependent on the crystal plane and the polar plane {0001} is the high active site for photocatalytic performance [16–19]. For another thing, significant efforts have been devoted to enhancing the photocatalytic performance and suppressing the photocorrosion by surface modification, such as combination with another semicon-

ductor, deposition of noble metals, and coupling with versatile carbon materials [20–27].

To evaluate the inhibitory effect of photocorrosion, the photocatalytic stability during the recycled degradation is employed all in this work [19,23,28]. It is demonstrated that less declination of photocatalytic efficiency means more effective suppression of photocorrosion. Then, a significant question arises: is the photocatalytic stability only related to the photocorrosion for ZnO? As previous work reported, many photocatalysts also suffer the stability, such as g-C<sub>3</sub>N<sub>4</sub>, black TiO<sub>2</sub>, WO<sub>3</sub> and so on [29–31]. These work indicates that the serious agglomerates, unstable defect, loose loading of metal and doping content loss all could be considered as the factors that influence the stability of photocatalyst as well as the photocorrosion. Similarly, could there be several factors attributed to the decrease of photocatalytic activity of ZnO during the recycled irradiation? Thus, the corresponding effect of photocorrosion on the photocatalytic stability should be further investigated. Meanwhile, what are other factors and how they influence the stability, which should also be studied.

Recently, two-dimensional porous nanosheet-like ZnO has attracted great research interests [32–35] due to its large surface-to-volume ratio, which can significantly enhance properties in photocatalysis. Instead of the focus on photocatalytic activity, in

\* Corresponding author at: Key Laboratory for Special Function Materials and Structure Design of the Ministry of Education, Lanzhou University, Lanzhou 730000, PR China.

E-mail address: [wuh@lzu.edu.cn](mailto:wuh@lzu.edu.cn) (Y. Wang).

this work, the influence of the factors on stability was investigated for the porous ZnO nanosheets. Apart from the photocorrosion, a phenomenon of photocatalytic reaction-induced selective corrosion was firstly revealed. Then, this special corrosion performances were compared with the photocorrosion and their impacts on morphology and photocatalytic stability were presented.

## 2. Experimental

### 2.1. Sample preparation

ZnO was prepared by surfactant-free hydrothermal method using  $\text{Zn}(\text{Ac})_2 \cdot 2\text{H}_2\text{O}$  and  $\text{CO}(\text{NH}_2)_2$ . In a typical synthesis, 0.5 mmol  $\text{Zn}(\text{Ac})_2 \cdot 2\text{H}_2\text{O}$ , 0.5 mmol  $\text{CO}(\text{NH}_2)_2$  were dissolved in 50 mL deionized water and were stirred for 20 min to form a clear solution, then the solution was transferred into a 100 mL Teflon-lined stainless steel autoclave and heated at  $160^\circ\text{C}$  for 10 h. The precursor was centrifuged and washed several times with deionized water and absolute ethanol, and then dried at  $60^\circ\text{C}$  for 12 h. Finally, the precursor was calcined at  $550^\circ\text{C}$  for 4 h in air with the heating rate of  $4^\circ\text{C}/\text{min}$ .

Ag was loaded on the ZnO nanosheets through impregnation and reduction method. In a typical synthesis, 0.12 g ZnO nanosheets were soaked into 30 mL 12.5 mM silver nitrate ( $\text{AgNO}_3$ ) solution and the mixture was stirred for 30 min and ultrasonicated for 20 min. Then the  $\text{Ag}^+$  modified ZnO was collected and washed with water for one time. The reduction of  $\text{Ag}^+$  on ZnO was achieved by impregnating the above collection into 20 mL 0.15 M  $\text{NaBH}_4$  solution and the final product Ag loaded ZnO was obtained through washing with water for several times and then drying at  $60^\circ\text{C}$  for 10 h.

### 2.2. Sample characterization

X-ray diffraction (XRD) experiments were carried out with a D/max-2400 diffractometer (Rigaku, Japan) using Cu-K $\alpha$  radiation. The morphologies were examined by scanning electron microscopy (SEM, Hitachi S-4800 and S-3400), high-resolution transmission electron microscope (HRTEM, Tecnai<sup>TM</sup> G2 F30, FEI, US), high angle annular dark field and scanning transmission electron microscopy (HAADF-STEM). Diffuse reflectance ultraviolet-visible (UV-vis) absorption spectra were measured by a PerkinElmer Lambda 950 spectrometer in the region of 200–700 nm, while  $\text{BaSO}_4$  was used as a reference. Atomic absorption spectrometry AA240 was used for the determination of  $[\text{Zn}^{2+}]$ . X-ray photoelectron spectroscopy (XPS) was conducted on a Kratos AXIS Ultra DLD spectrometer.

### 2.3. Evaluation of photocatalytic activity

The photocatalytic activity of samples was measured by the decomposition of methylene blue (MB) solution in a reactor at room temperature. In a typical process for degradation, 40 mg of photocatalyst was suspended in the MB solution (10 mg/L, 80 mL). Before irradiation, the suspensions were stirred for 30 min in the dark to ensure the establishment of adsorption-desorption equilibrium. A 500 W high-pressure mercury lamp was employed for the ultraviolet (UV) light irradiation source which was positioned 20 cm away from the reactor to trigger the photocatalytic reaction. A certain volume of suspension was withdrawn at selected times for analysis. After recovering the photocatalyst by centrifugation, the concentration of dye solution was analyzed by measuring the light absorption of the clear solution at 664 nm ( $\lambda_{\text{max}}$  for MB solution) using a spectrophotometer (WFJ-7200, Unico, USA). The percentage of degradation was calculated by  $C/C_0$ . Here,  $C$  is the concentration of remaining dye solution at each irradiated time interval, while  $C_0$  is the initial concentration.

To investigate the active species generated in the photocatalytic degradation process, the experiments of active species (hydroxyl radical ( $\cdot\text{OH}$ ), hole ( $\text{h}^+$ ) and  $\cdot\text{O}_2^-$ ) capture were carried out by using *t*-butyl alcohol and ethylenediamine tetraacetic acid disodium salt (EDTA-2Na) and purging  $\text{N}_2$  under UV light irradiation [32,36], respectively. The amounts of added *t*-butyl alcohol and EDTA-2Na are 5.9 mg (1 mM) and 29.8 mg (1 mM), respectively, and the flow velocity of  $\text{N}_2$  is 1 L/min [32].

Hydroxyl radicals ( $\text{OH}\cdot$ ) produced during photocatalysis were estimated by the fluorescence method using terephthalic acid (TA) as a probe molecule [37]. In a typical process, 40 mg photocatalyst was dispersed in 80 mL aqueous or MB solution with TA ( $5 \times 10^{-4}$  M) and NaOH ( $2 \times 10^{-3}$  M). The resulting suspension was exposed to UV light irradiation and at regular intervals, 3.0 mL of the suspension was collected and centrifuged. Then, the maximum fluorescence emission intensity measured with an excitation wavelength of 315 nm. This method relies on the fluorescence signal at 425 nm of the 2-hydroxyterephthalic acid (TAOH).

## 3. Results and discussion

### 3.1. Phenomenon of photocatalytic reaction-induced selective corrosion

Firstly, XRD patterns, XPS spectra and the photocatalytic activity of fresh Ag-ZnO and ZnO were investigated, as shown in Fig. 1.

XRD patterns of fresh ZnO in Fig. 1(a) indicate that all peaks of the ZnO can be indexed (JCPDS card No. 36-1451) very well, and no peaks of other impurities can be detected. For Ag-ZnO, there are three peaks at  $38.1^\circ$ ,  $44.2^\circ$  and  $64.4^\circ$ , corresponding to (111), (200) and (220) planes of the Ag nanoparticles (JCPDS card No. 04-0783), respectively, which indicates the obtained composition of Ag-ZnO. XPS spectra were employed to clarify the chemical state of Ag in the Ag-ZnO nanocomposite, and high resolution XPS spectrum of Ag 3d is shown in inset of Fig. 1(b). There are two adjacent peaks at 367 eV and 373 eV, which correspond to Ag 3d $_{3/2}$  and Ag 3d $_{5/2}$ , respectively, indicating a metallic nature of silver. Compared with the standard value of bulk Ag, the 3d peak of Ag shifts to lower binding energy due to the intense interaction between Ag and ZnO nanocrystals. From Fig. 1(c), it can be seen that the photocatalytic activity of Ag-ZnO is much higher than that of pure ZnO. The kinetics of photocatalytic reactions can be described using a first order reaction, as displayed in inset of Fig. 1(c). The apparent rate constant ( $k$ ,  $\text{min}^{-1}$ ) of Ag-ZnO is  $0.234 \text{ min}^{-1}$ , which is enhanced compared with that of ZnO. In addition, the photocatalytic activities of Ag-ZnO are also higher than that of ZnO for degradation of MO and RhB solution as well as MB solution, as shown in Fig. 1(d). Therefore, the introduction of Ag nanoparticles can increase the photocatalytic activity of ZnO.

The above increase of photocatalytic activity for Ag-ZnO is kept in recycled photocatalytic measurement, as shown in Fig. 2. The decrease of photocatalytic activity is not obvious within 3 recycles. The Fig. S1 (ESI<sup>†</sup>) shows the XPS spectra of fresh Ag-ZnO and Ag-ZnO after run 1, 2, 3 in MB solution under UV light irradiation. It can be seen that the peaks of Ag 3d and O 1s do not change during the recycled UV light irradiation, which indicates the same chemical situations of Ag and O within run 3. However, from the inset of Fig. 2, it can be observed that the morphological change (the pore shape change) occurs in run 2 and becomes more obvious in run 3 both for Ag-ZnO and ZnO. In general, the morphological collapse of ZnO is attributed to the photoinduced dissolution, i.e., photocorrosion, which mainly leads to the decreased activity for ZnO photocatalyst [24]. According to the above observation, the decrease of recycled photocatalytic activity is unobvious while the photoinduced etching has been proceeded. Thus, it is necessary

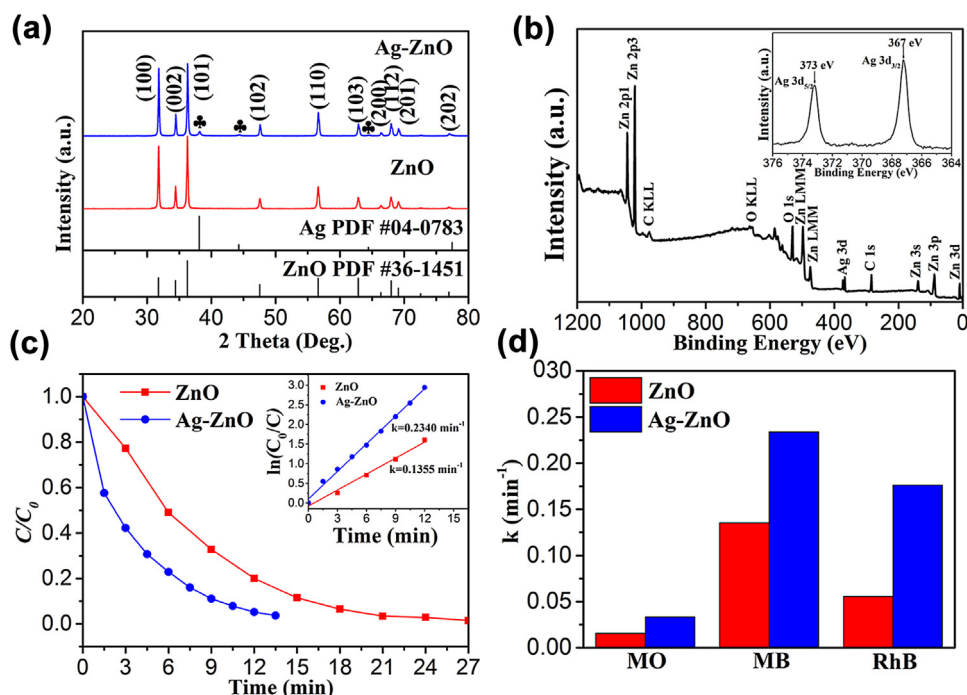


**Fig. 1.** (a) XRD patterns of Ag-ZnO and ZnO; (b) XPS spectrum of Ag-ZnO; (inset) high resolution XPS spectrum of Ag 3d; (c) photocatalytic activity of Ag-ZnO and ZnO; (inset) plots of  $\ln(C_0/C)$  versus irradiation time for MB solution representing the fit using a pseudo-first-order reaction rate; (d) fitted reaction rate  $k$  comparison of Ag-ZnO and ZnO in MO, MB and RhB solution.

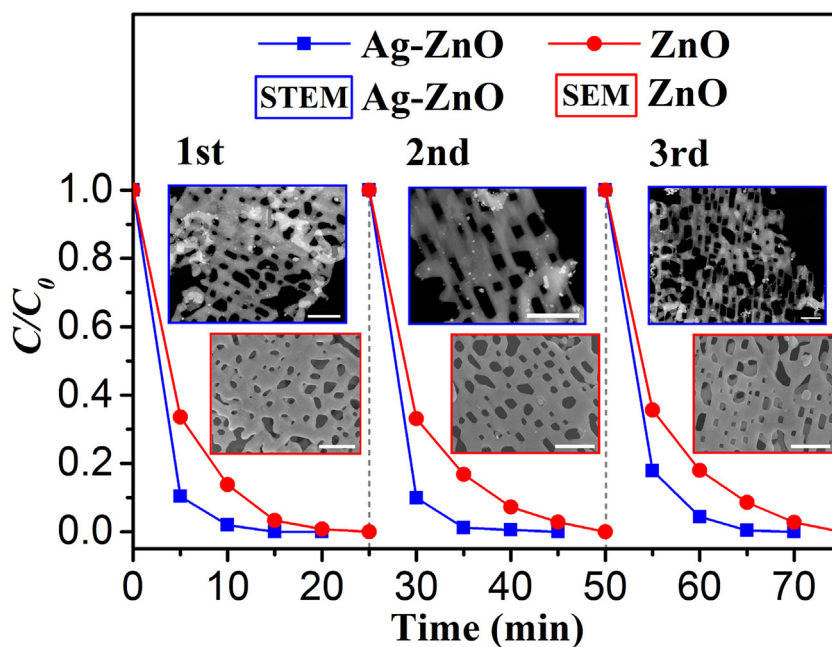


**Fig. 2.** Recycled photocatalytic measurement of Ag-ZnO and ZnO for MB solution and (inset) corresponding morphologies change of Ag-ZnO and ZnO. The all scale bars are 500 nm.

to make the relationship between them more clear. In the following parts, the recycled time dependent morphological change is investigated.

### 3.2. Morphological change comparison

Compared with fresh Ag-ZnO in Fig. 3(a), the irregular pores almost change into the uniform quasi-rectangle pores after run 3 in MB solution under UV light irradiation, as shown in Fig. 3(b).

Since the etching is selective, there is a hypothesis that the morphological collapse may be attributed to a special corrosion in MB solution rather than the photocorrosion, which is labeled as photocatalytic reaction-induced selective corrosion (PRIS corrosion) and demonstrated as follows.

In order to further investigate the morphological change, Ag-ZnO and ZnO were irradiated under UV light in MB solution for more recycle times. After run 6, the selective etching can be observed easily for ZnO collected from MB solution, as shown in Fig. 4(a1–a4).



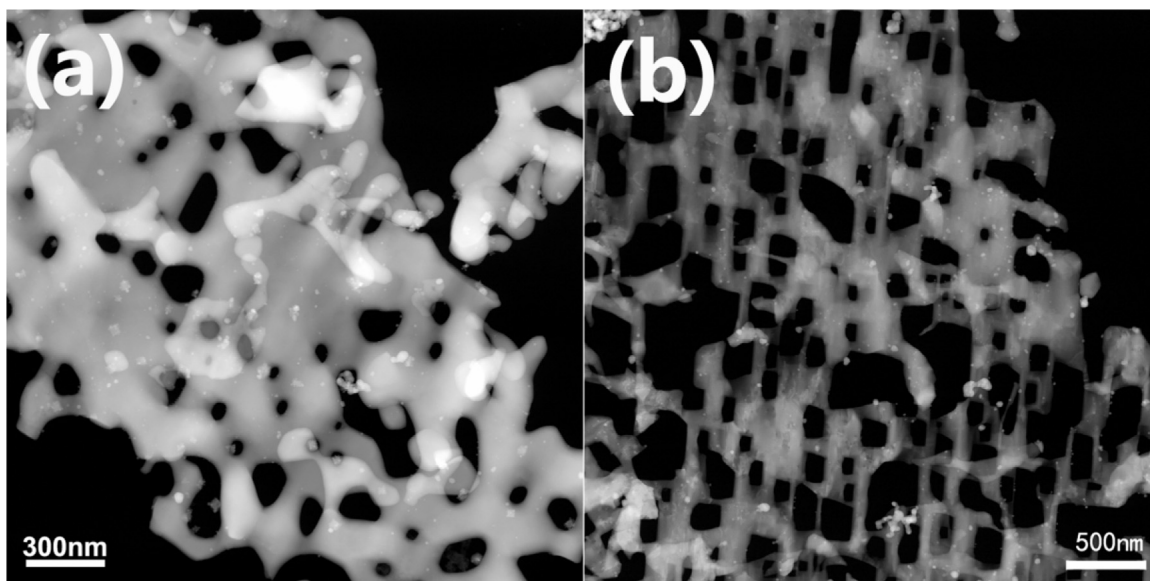


Fig. 3. STEM images of fresh sample Ag-ZnO (a) and Ag-ZnO after run 3 in MB solution (b) under UV light irradiation.

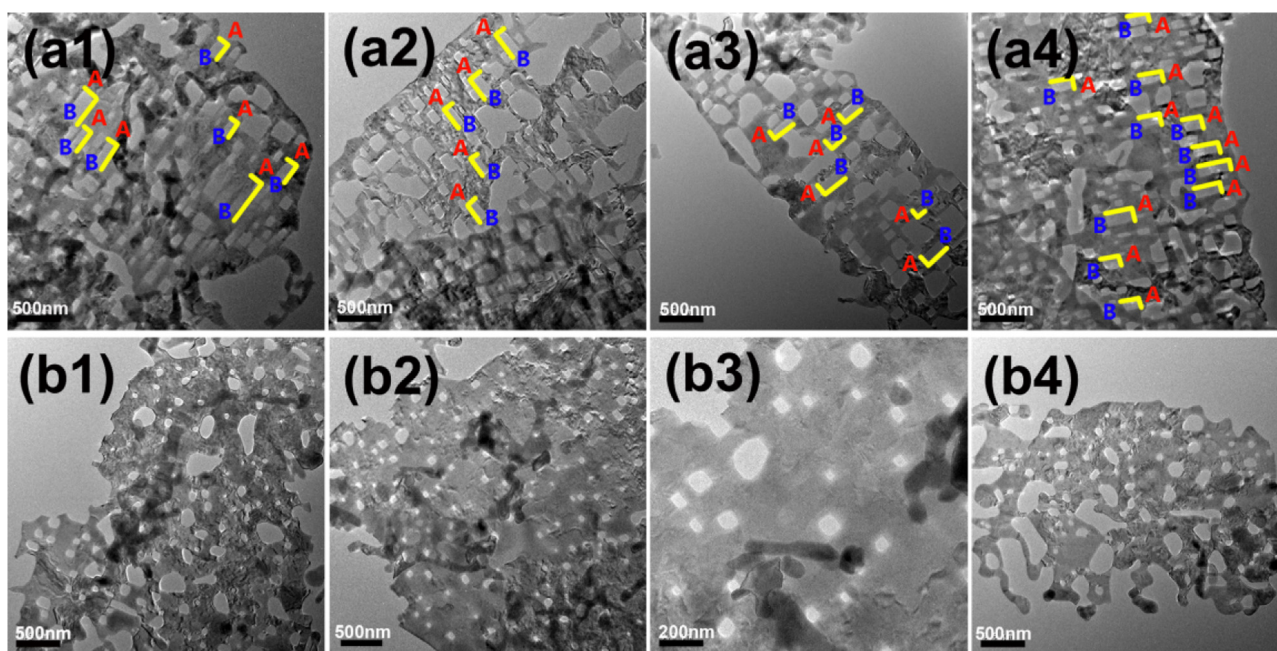


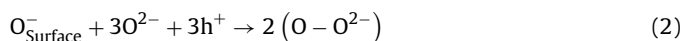
Fig. 4. TEM images at four sites of ZnO after run 6 in MB solution (a1–a4) and water (b1–b4) under UV light irradiation.

The rectangle pores consist of short side A and long side B. To verify the role of MB solution, samples were also irradiated in water. After the same cycles, the etching of the pores is hardly to be found for ZnO collected from water. This contrasting results keep the same rule for Ag-ZnO collected from MB solution and water, as shown in Fig. S2. Thus, it indicates that the corrosion of sample collected from MB solution is more obvious and selective than that of sample collected from water.

After run 10, the SEM images of the collected samples are shown in Fig. 5. It can be seen that there is an obvious selective etching in Ag-ZnO and ZnO after run 10 times in MB solution. In contrast, they keep initial morphology or show slight non-selective corrosion after run 10 times in water instead of MB solution. In addition, the control group was conducted in MB solution in dark for 24 h, as shown in Fig. S3. It can be seen that Ag-ZnO and ZnO present

their initial morphology without UV light irradiation. The above results indicate that the special corrosion not only needs MB solution, but also require the UV light irradiation. Namely, the visual and selective change of pores in MB solution could be attributed to the photocatalytic degradation reaction, which is different from the photo-induced photocorrosion.

According to previous reports [24], the photocorrosion of ZnO consists of two slow steps and followed by two fast steps, which can be described as following.



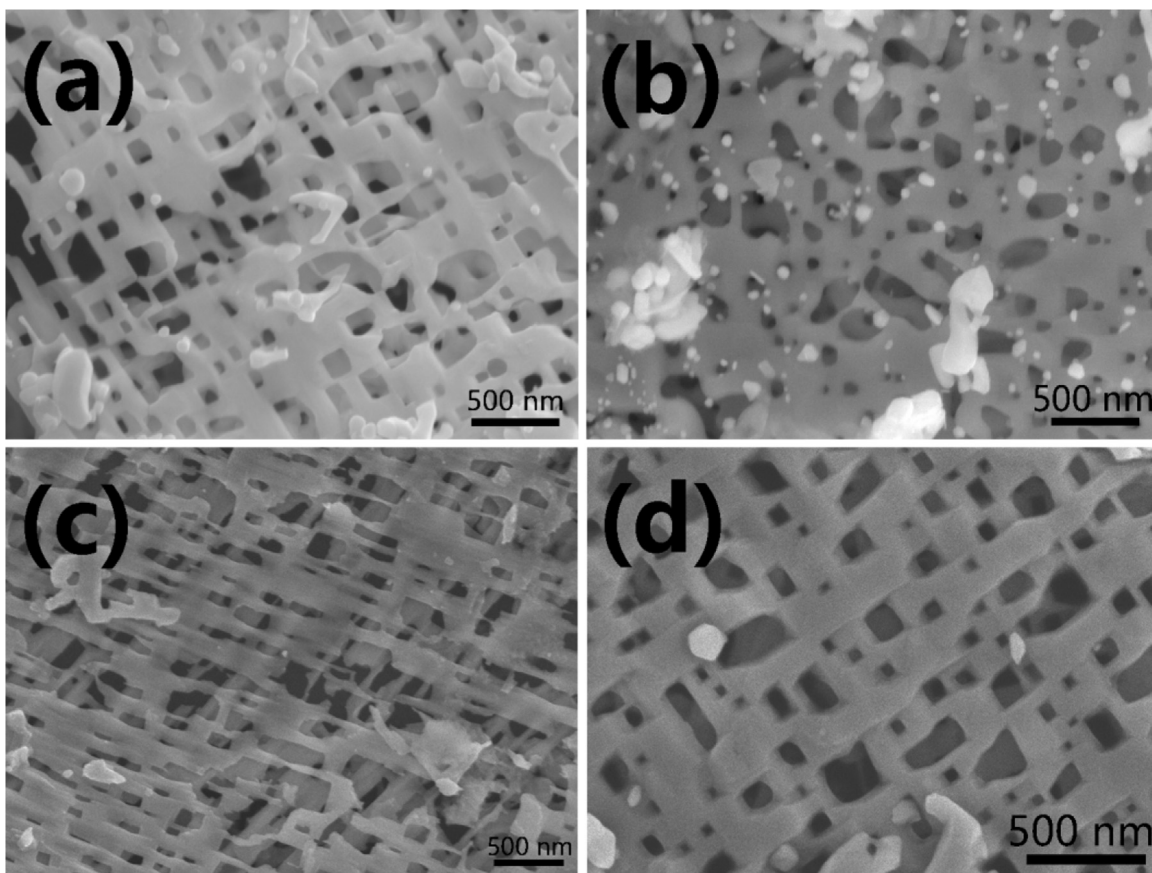


**Fig. 5.** SEM images of Ag-ZnO after run 10 in MB solution (a) and in water (b) under UV light irradiation; SEM images of ZnO after run 10 in MB solution (c) and in water (d) under UV light irradiation.

The overall reaction for dissolution of ZnO can be expressed as follow:



Thus, the photogenerated  $\text{h}^+$  could be the main reason for photocorrosion of the ZnO. However, in MB solution,  $\text{h}^+$  is not only the suspect guilty of the morphological collapse of ZnO, but also the decisive oxidative species leading to the high photocatalytic activity. These photogenerated  $\text{h}^+$ -induced corrosion and photodegradation occur simultaneously and these two competitive processes could occur around the same active site, leading to the above special selective corrosion.

To verify this inference, the oxidative species contributions are investigated. In Fig. 6(a), the plots of photodegradation by the ZnO in MB solution are presented under UV light irradiation adding *t*-butyl alcohol, EDTA-2Na,  $\text{N}_2$  as the photoinduced carriers trapping. It is found that the photocatalytic activity of ZnO decreases slightly by the addition of *t*-butyl alcohol ( $\bullet\text{OH}$  scavenger) and reduces largely with the addition of EDTA-2Na ( $\text{h}^+$  scavenger). This indicates that the photogenerated  $\text{h}^+$  rather than the  $\bullet\text{OH}$  is the decisive oxidative species for ZnO. Like previous reports [38], when purging  $\text{N}_2$  ( $\text{O}^{2-}$  scavenger), the MB solution can be photoreduced to colorless leuco-methylene blue (LMB), while it is recovered when purging  $\text{O}_2$ , as shown in the inset of Fig. 6(a). It means that purging  $\text{N}_2$  into MB solution or other reductants can not be used to determine the role of  $\text{O}_2$ . Since ZnO suffers the same selective corrosion in RhB solution, as shown in Fig. S4, the RhB is employed as the new degradation target and the results are shown in Fig. 6(b). It can be seen that the degradation efficiency of Ag-ZnO reduces largely with the addition of EDTA-2Na, and decreases slightly by the addition of

*t*-butyl alcohol, which is in consistent with the rule of ZnO in MB solution. This indicates that the photogenerated  $\text{h}^+$  rather than the  $\bullet\text{OH}$  is the decisive oxidative species for Ag-ZnO as well as ZnO. Furthermore, the photocatalytic activities of Ag-ZnO and ZnO both decrease when purging  $\text{N}_2$ , which means the oxygen influences the photocatalytic activity. Therefore, the photogenerated  $\text{h}^+$  and  $\text{O}^{2-}$  are the main active oxidative species in photocatalytic process for ZnO and the introduction of Ag into ZnO keeps the same rule. With the same species, these two competitive processes, corrosion and degradation, could occur around the same active site, leading to the above special selective corrosion.

Although Ag-ZnO undergo these two competitive processes as well as ZnO, there is something different between them. It is found in Fig. 5 that the Ag-ZnO shows less etching compared with pure ZnO both in water and in MB solution, which suggests the inhibitory effect of corrosion by loading Ag on ZnO. From Table 1, it is found that the ratios of decreased photocatalytic activities for Ag-ZnO are lower than that for ZnO when adding scavengers. This results indicate that the oxidative species contribution may change a little when loading Ag on ZnO, especially for  $\bullet\text{OH}$ . To verify the contribution alteration of  $\bullet\text{OH}$  in the current system, a terephthalic acid (TA) probe was used, whereby reaction of TA with  $\text{OH}^\bullet$  radicals to generate fluorescent 2-hydroxyterephthalic acid (TAOH) was monitored.

**Table 1**

Decline ratio of photodegradation efficiency in MB solution for Ag-ZnO under UV light irradiation when adding scavengers.

Decline ratio (%)	$\text{h}^+$ scavenger	$\bullet\text{OH}$ scavenger	$\text{O}^{2-}$ scavenger
ZnO	94	28	48
Ag-ZnO	71	2	33

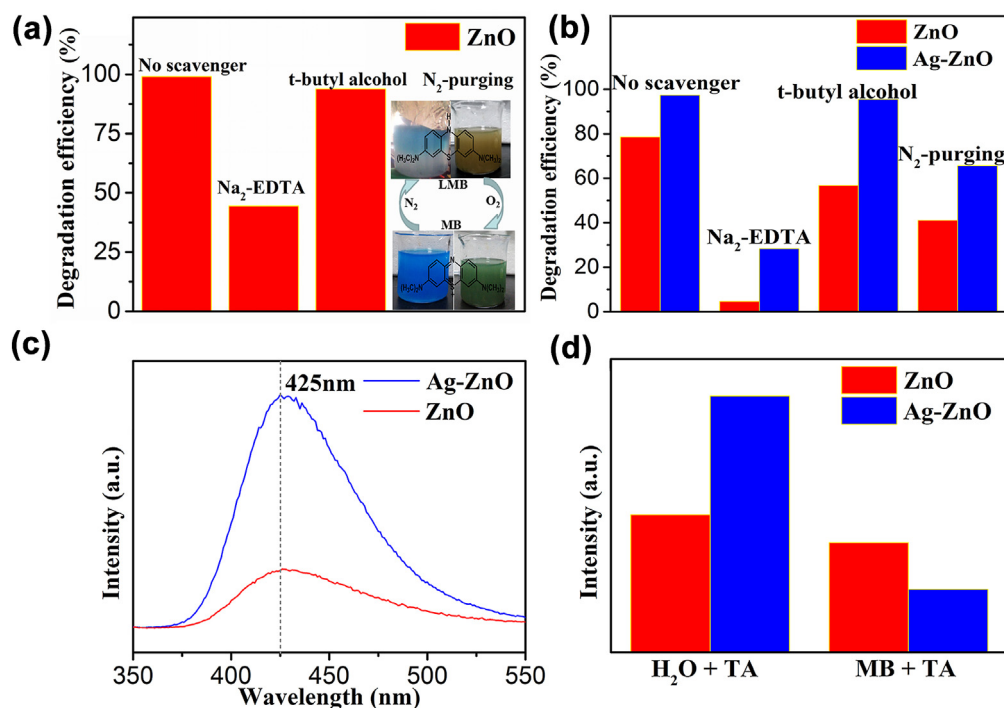


**Fig. 6.** (a) Degradation efficiency of MB solution by using different radical scavengers for ZnO; (b) degradation efficiency of RhB solution by using different radical scavengers for Ag-ZnO and ZnO; (c) fluorescence spectra measured after illumination 5 min of Ag-ZnO and ZnO in a basic solution of TA (excitation at 315 nm); (d) fluorescence spectra intensity comparison measured after illumination 5 min of Ag-ZnO and ZnO in a basic solution of TA + H<sub>2</sub>O and TA + MB solution (excitation at 315 nm).

After UV light irradiation for 5 min in water, the maximum intensity at 425 nm of TAOH produced by Ag-ZnO was much higher than that of pure ZnO upon excitation at 315 nm, as shown in Fig. 6(c). This result indicates that more  $\cdot\text{OH}$  radicals are generated by Ag-ZnO compared with pure ZnO in water.

In contrast, the rule changes when the TAOH is monitored in MB solution, as shown in Fig. 6(d). The fluorescent intensity of TAOH produced by pure ZnO changes little while it decreases largely for Ag-ZnO in MB solution. As the enhanced activity of Ag-ZnO is mainly owing to the photogenerated  $\text{h}^+$  but not  $\cdot\text{OH}$ , the large decrease of  $\cdot\text{OH}$  in MB solution could be attributed to the higher use efficiency of photogenerated  $\text{h}^+$ . Therefore, the competitive processes in MB solution make the oxidative species contribution different from that in water due to the photocatalytic reaction. That is to say, the special corrosion and photodegradation occur simultaneously around the same active site, which make the PRIS corrosion in MB solution differ from the photocorrosion in water.

To identify the mechanism of the above selective corrosion during the degradation in MB solution, TEM is used to observe the pore in the ZnO nanosheets. It can be seen from Fig. 7(a), the initial nonuniform pores almost change into rectangle. One side is labeled as "a" and the other is labeled as "b". The HRTEM image shows the lattice fringes of edge a and b around the pore, as shown in Fig. 7(b–c). The lattice spacing is 0.26 nm and 0.16 nm, corresponding to the (002) and (110) planes of ZnO, respectively. The selected area electron diffraction (SAED) pattern of ZnO nanosheets in Fig. 7(d) presents the diffraction spots, thereby revealing the monocrystalline nature of ZnO nanosheets. It is identified that the crystal face of nanosheets is assigned to (100), and the vertical planes are (002) and (110). According to the above results, it can be concluded that the face of (002) is easy to be etched owing to its active activity in photocatalytic degradation under UV light irradiation. Fig. 7(e1)–(e4) show the formation process of rectangular pore. Compared with the ideal crystal of ZnO in Fig. 7(e1), there is a pore on the plane (100) of porous ZnO, as shown in Fig. 7(e2). Owing

to the active activity of the plane (002), where the degradation reaction induces the enrichment of  $\text{h}^+$ , the corrosion site mainly focus on the active plane, as shown in Fig. 7(e3). Then, it is reasonable that the selective corrosion is observed along the direction of [0001] as shown in Fig. 7(e4). Thus, the schematic of the morphological change after PRIS corrosion can be presented as shown in Fig. 7(f). It can be seen that the one side corresponding to the plane (002) around the pores is etched thus the rectangle pores are formed after PRIS corrosion. Moreover, the schematic diagrams of inhibitory effect against PRIS corrosion are shown in Fig. 7(g). As X. Jin et al. and Q. H. Li et al. reported, the photoexcited electron transfer rate represents one of the most important properties [39,40]. When the electron transfer life time was shortened, a notable enhancement of power conversion efficiency could be achieved. In the Ag-ZnO system, the as-excited electrons can be rapidly transferred from ZnO to Ag nanoparticles due to the deflexed energy band in the space charge region as shown in Fig. 7(g), which suppress the recombination of the photogenerated pairs [39–43]. Due to the rapid transfer of photoexcited electrons to Ag, the photoinduced  $\text{h}^+$  can be more effective to react with organic dye, which leading to the suppression of selective corrosion. Therefore, the loaded Ag can restrain the corrosion and enhance the photocatalytic stability due to the advantage of more useful  $\text{h}^+$  for degradation and less for corrosion in Ag-ZnO over pure ZnO.

In addition to the morphological change, the impacts of the above two kinds of corrosion on the Ag-ZnO itself are presents in Fig. 8. As shown in Fig. 8(a), the peaks of Ag in XPS spectra after run 10 in MB solution shift slightly to lower banding energy compared with that of fresh Ag-ZnO. According to the SEM observation in Fig. 5(a), the shift to lower binding energy could be attributed to close interaction between Ag and ZnO after run 10 in MB solution [41,43]. In contrast, the peaks of Ag shift to higher binding energy after run 10 in water. This could be due to the aggregation of small Ag nanoparticles into big particle, as shown in Fig. 5(b), which become more close to the high binding energy of bulk Ag. Besides



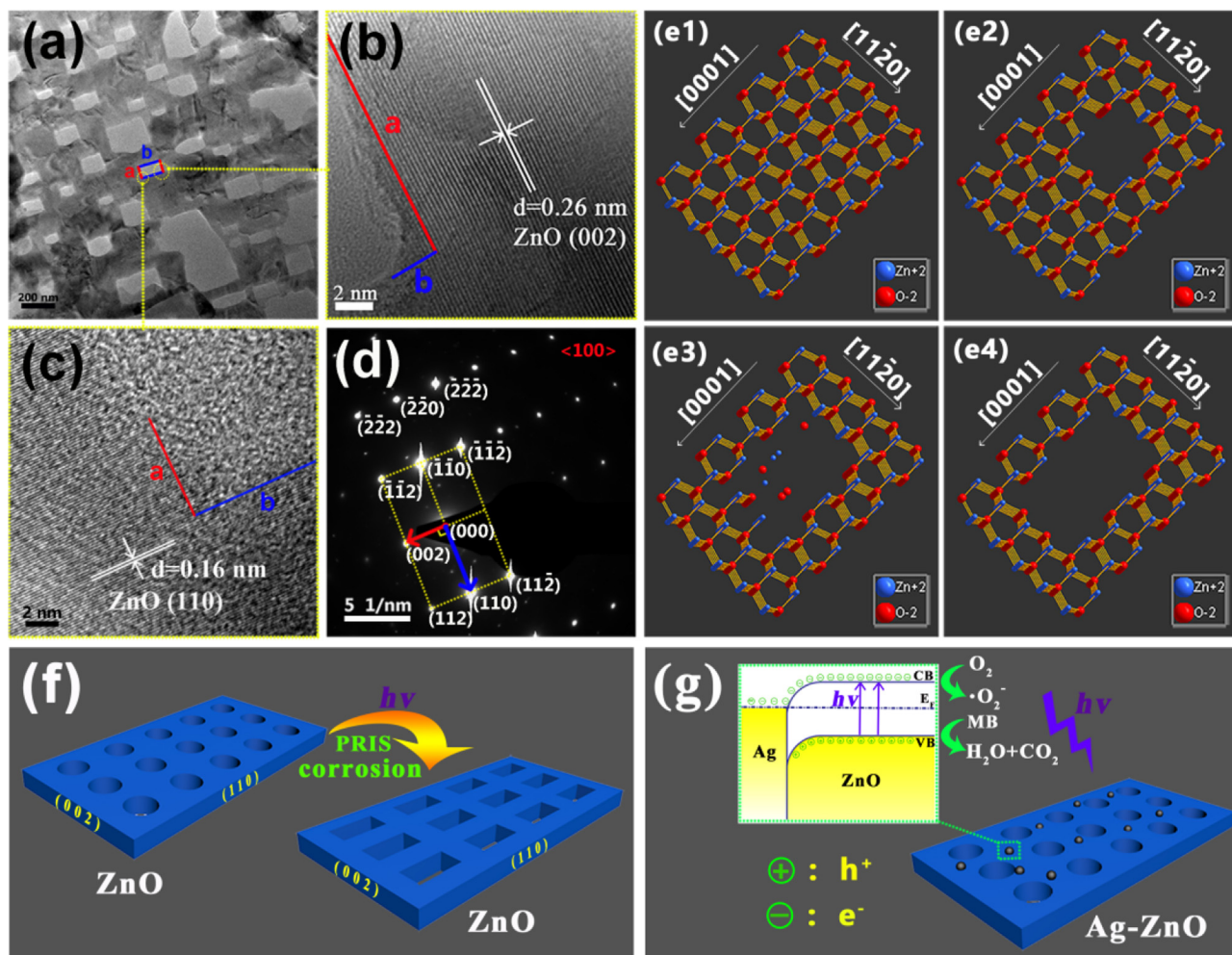
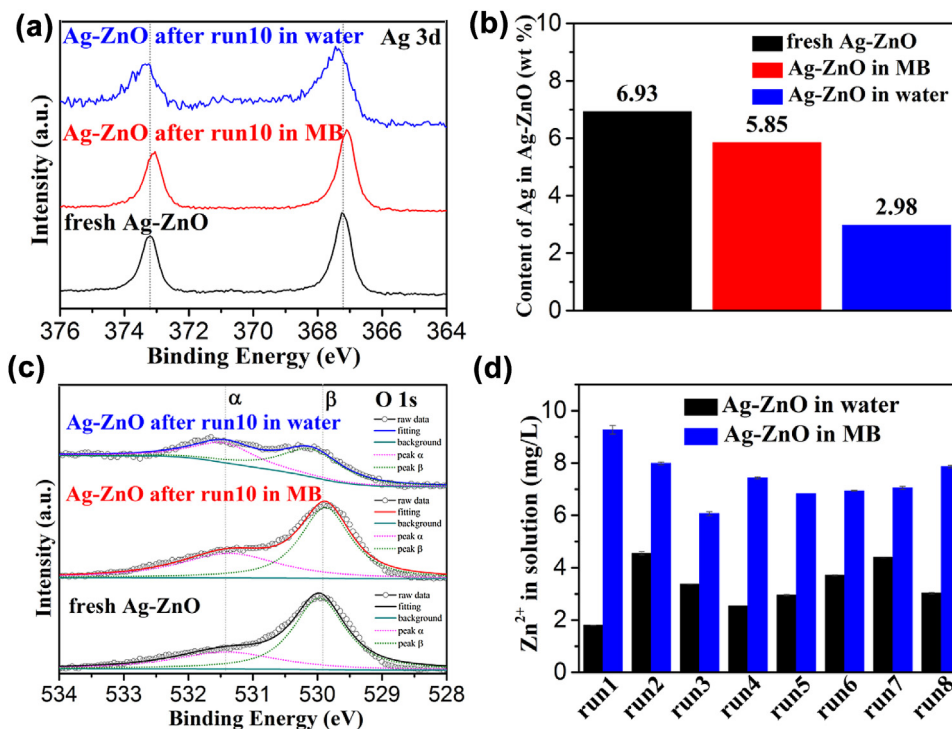


**Fig. 7.** TEM image (a) of ZnO and HRTEM images around edge a and edge b (b–c); (d) SAED pattern of Ag-ZnO; (e1–e4) illustration of formation process of rectangular pore; (f) schematic of the morphological change after PRIS corrosion; (g) schematic diagram of inhibitory effect against PRIS corrosion of Ag-ZnO under UV light.

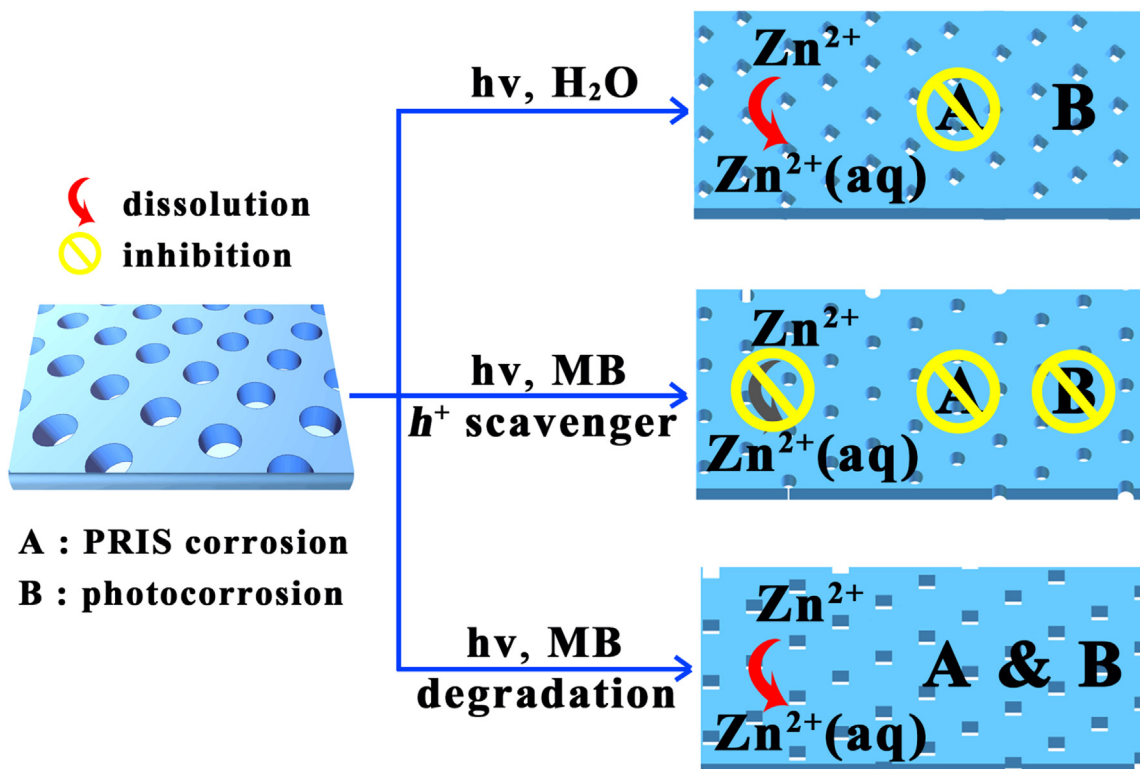
the size change of Ag particles, the contents of Ag also decrease in varying degrees, as shown in Fig. 8(b). Compared with the fresh Ag-ZnO, the content of Ag after run 10 in MB solution declines slightly from 6.93% to 5.85%, which is benefited from the close contact between Ag and ZnO. However, after run 10 in water, the content of Ag falls to 2.98%, which indicate the more loss of Ag. In Fig. 8(c), O 1s profiles are asymmetric and can be fitted into two symmetrical peaks  $\alpha$  and  $\beta$ , which implies the presence of two different kinds of O species. The peak  $\alpha$  located at 531.4 eV and the peak  $\beta$  located at 529.9 eV, are associated with the chemisorbed oxygen of the surface hydroxyls and lattice oxygen of ZnO, respectively [43]. Compared with the fresh Ag-ZnO, the peak  $\alpha$  at 531.4 eV increases dramatically after run 10 in water while it changes a little after run 10 in MB solution. Besides the elements of Ag and O, the high resolution Zn 2p spectra are presented in Fig. S5. Unlike the recovered Ag-ZnO from MB solution and the fresh Ag-ZnO, the original doublet peak splits up into a quartet peak in total for the sample recovered from water. The doublet peak at 1021 and 1044 eV is attributed to Zn atoms within the ZnO phase, while the other doublet peak at 1025 and 1049 eV is ascribed to Zn atoms at other phase. The splitting of the original doublet peak indicates the possible interfacial hybridization between ZnO phase and other phase [44], which is in consistent with the above change of O 1s. Moreover, the comparison of Zn<sup>2+</sup> loss in every run is shown in Fig. 8(d). It is found that the Zn<sup>2+</sup> loss in MB solution is higher than that in water during run 1 to run 8, which leads to more obvious corrosion as shown in

Fig. 6. According to the above results, it is concluded that the Zn<sup>2+</sup> loss at the active face is the main change after PRIS corrosion in MB solution, while the varying composition and Ag size are almost simultaneous with little Zn<sup>2+</sup> loss after photocorrosion in water.

Therefore, the above comparison of morphological change together with the mass change reveals the different features between the PRIS corrosion and photocorrosion. Under each of the three situations as illustrated in Fig. 9, it is presented respectively that whether two kinds of corrosion occur and what the results of the morphological change of ZnO nanosheets. When sample is irradiated under UV light in water, photocorrosion occurs alone, which leads to the loss of Zn<sup>2+</sup> and nonselective morphological change. In contrast, PRIS corrosion together with photocorrosion both take place when the sample is irradiated under UV light in MB solution. It indicates that the UV light irradiation is the common condition of two kinds of corrosion, but the PRIS corrosion only occurs under the photocatalytic reaction. Under this situation, loss of Zn<sup>2+</sup> and selective etching around the active face occurs simultaneously together with the degradation reaction in MB solution. When the above degradation reaction is repressed by adding scavengers into MB solution, PRIS corrosion and photocorrosion both are almost vanished, as shown in Fig. S6. Then, it can be concluded that the photocorrosion occurs when the  $h^+$  is photogenerated and it leads to the mass loss. Besides the photogenerated  $h^+$ , the PRIS corrosion appears when the  $h^+$  reacts with organic dye and it results in the loss of active face and the selective corrosion.



**Fig. 8.** XPS spectra of fresh Ag-ZnO, Ag-ZnO after run 10 in MB solution, Ag-ZnO after run 10 in water: (a) Ag 3d; (c) O 1s; (b) content comparison of Ag in XPS of Ag-ZnO; (d) concentration of  $\text{Zn}^{2+}$  in solution for Ag-ZnO during run 1 to run 8 by irradiated in water and MB solution.



**Fig. 9.** Schematic illustration of the morphology change comparison between the PRIS corrosion and photocorrosion for the porous ZnO nanosheets.

Then, a question arises: what is the next story when the impacts of two kinds of corrosion show different features? Will they present different influences on the photocatalytic stability? In the follow-

ing part, their impacts on photocatalytic stability are investigated, including recycled stability and recovered stability.



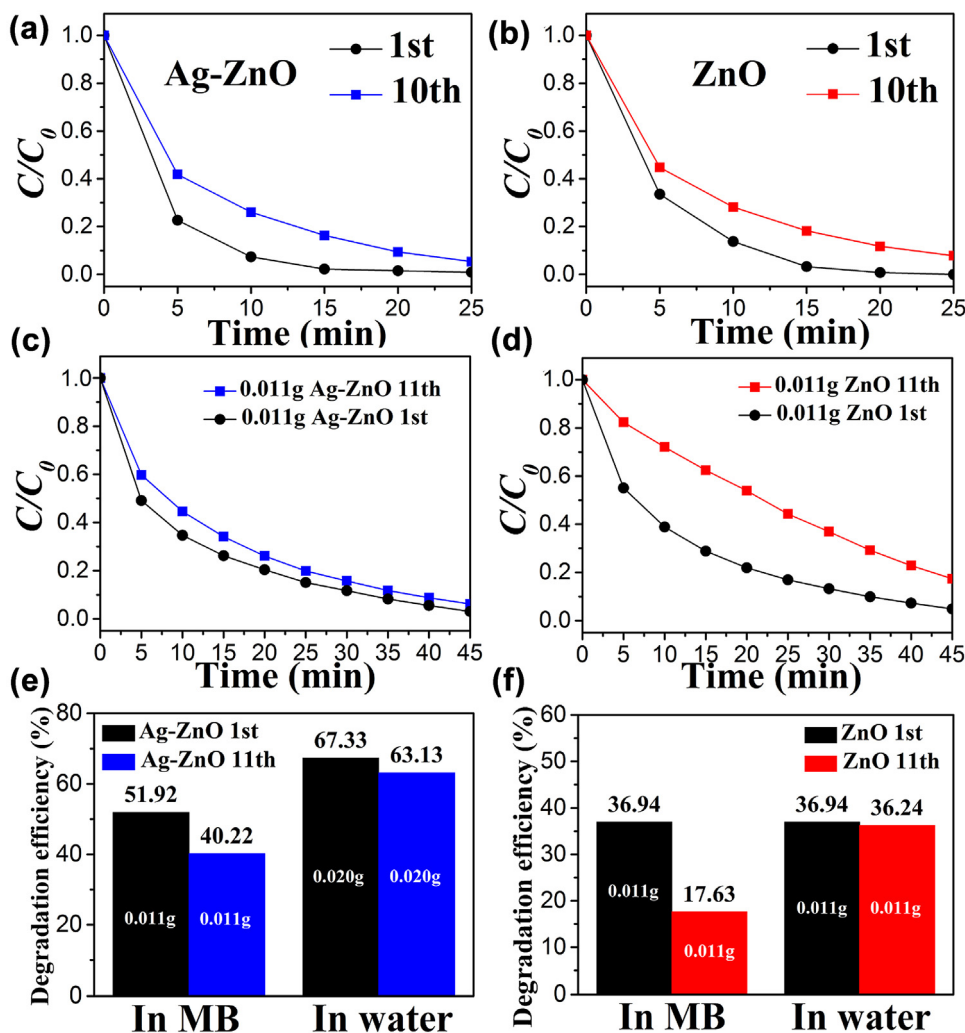


**Fig. 10.** Photocatalytic activity of the Ag-ZnO (a) and ZnO (b) at run 1 and run 10 in MB solution under UV light irradiation; (c) photocatalytic activity comparison with the same mass between the fresh Ag-ZnO and the recovered Ag-ZnO after run 10 in MB solution; (d) photocatalytic activity comparison with the same mass between the fresh ZnO and the recovered ZnO after run 10 in MB solution; degradation efficiency comparison of Ag-ZnO (e) and ZnO (f) between fresh sample and recovered sample with the same mass after corrosion in MB solution and in water under UV light irradiation for 5 min.

### 3.3. Impacts on photocatalytic stability

To investigate the influences of two kinds of corrosion on the photocatalytic stability, the photocatalytic activities of recycled and recovered samples are measured. As shown in Fig. 10(a), the Ag-ZnO after recycle for 10 times in MB solution shows decreased photocatalytic activity compared with that of fresh Ag-ZnO. The similar result is obtained for ZnO in Fig. 10(b). The decrease of recycled activity could be attributed to several factors, such as the mass loss, the active face loss, the composition change and so on. To make the other factors more clear apart from the mass loss, the activities of recovered samples from MB solution and the fresh samples with the same mass are compared, as shown in Fig. 10(c,d). It can be seen that the decreases of activity still exist, especially for pure ZnO. This result indicates that the mass loss is one of the reasons for the recycled activity decrease but not the cause of the unit mass photocatalytic activity decline after PRIS corrosion in MB solution. Thus, it is concluded that the active face loss or others but not mass loss that determines the photocatalytic stability.

Since the impacts of two kinds of corrosion on morphological change show different features except mass loss, the unit mass photocatalytic activities of recovered samples from water were also measured, as shown in Fig. S7. It can be seen that the recovered

samples show almost the same unit mass activity compared with the fresh samples. This indicates that the mass loss but no others could be accounted for the decrease of recycled activity after photocorrosion in water. As shown in Fig. 10(e), compared with the same mass of fresh Ag-ZnO, the degradation efficiency of Ag-ZnO recovered after run 10 in MB solution decrease even more than that of the recovered Ag-ZnO after run 10 in water. The distinguish of decrease of efficiency are more noticeable and evident for ZnO, as shown in Fig. 10(f). Compared with the same mass of fresh ZnO, the efficiency of the recovered ZnO from MB solution falls by more than half while it almost keeps the same efficiency for the ZnO recovered from water.

According to the above results, the two kinds of corrosion present different influences on the photocatalytic stability, as illustrated in Fig. 11. For one thing, the recycled activities both decrease after corrosion in MB solution and in water. For another thing, the recovered sample after PRIS corrosion in MB solution shows largely decreased activity than that after photocorrosion in water. Thus, the selective etching-induced active face loss of the PRIS corrosion in MB solution can be fatal for the photocatalytic stability. In contrast, the loss of  $Zn^{2+}$  together with little mass change in photocorrosion influences slightly on the stability of the recovered sample. Moreover, as the unit mass activity decrease of Ag-ZnO is

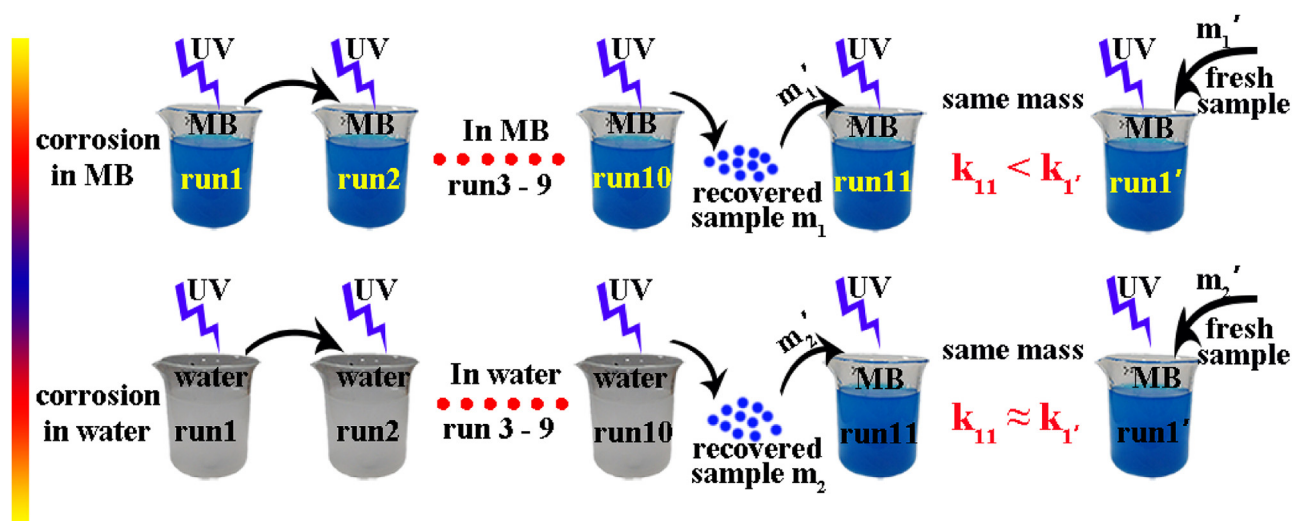


**Fig. 11.** Schematic diagram of the experimental operation of recycling runs, recovering samples after corrosion in MB solution and in water, and the comparison of unit mass photocatalytic activity with fresh samples.

not as noticeable as that of ZnO recovered from MB solution, there is the inhibitory effect of loaded Ag against selective corrosion thus leading to the high photocatalytic stability.

#### 4. Conclusion

In this work, a phenomenon of PRIS corrosion was firstly revealed in the degradation process of MB solution under UV light irradiation. This special visual corrosion not only needs UV light irradiation, but also results from the photocatalytic reaction. Furthermore, the PRIS corrosion shows more mass loss, more selective etching and more decrease of unit mass photocatalytic activity than that of photocorrosion. It is found that the selective corrosion-induced active face loss of the PRIS corrosion can be fatal for the photocatalytic stability. In contrast, the loss of  $\text{Zn}^{2+}$  in photocorrosion influences slightly on the stability of the recovered sample. Moreover, the loaded Ag can both restrain the two kinds of corrosion and enhance the photocatalytic stability due to the advantage of more useful  $\text{h}^+$  for degradation and less for corrosion in Ag-ZnO over pure ZnO. Therefore, the observation of two kinds of corrosion will throw new light on the relationship between corrosion and photocatalytic stability, and it can be a facile and interesting method to investigate the further modified samples for balancing the activity and stability.

#### Acknowledgements

This research was supported by the International Sci. & Tech. Cooperation Foundation of Gansu Provincial, China (Grant Nos 1504WKCA088 and 1304WCGA177), the National Science Foundation for Fostering Talents in Basic Research of National Natural Science Foundation of China (Nos 041105 and 041106), the National Natural Science Funds of China (Grant No. 51372105) and the Network Joint Research Center for Materials and Devices, the Grant-in-Aid for Science Research (No. 23241025).

#### Appendix A. Supplementary data

Supplementary data associated with this article can be found, in the online version, at <http://dx.doi.org/10.1016/j.apcatb.2016.08.029>.

#### References

- [1] L.G. Devi, R. Kavitha, Appl. Catal. B: Environ. 140–141 (2013) 559–587.
- [2] H. Xu, S.X. Ouyang, L.Q. Liu, P. Reunchan, N. Umezawa, J.H. Ye, J. Mater. Chem. A 2 (2014) 12642–12661.
- [3] F. Fresno, R. Portela, S. Suarez, J.M. Coronado, J. Mater. Chem. A 2 (2014) 2863–2884.
- [4] Z.W. Zhao, Y.J. Sun, F. Dong, Nanoscale 7 (2015) 15–37.
- [5] X. Li, J.G. Yu, J.X. Low, Yu P. Fang, J. Xiao, X.B. Chen, J. Mater. Chem. A 3 (2015) 2485–2534.
- [6] M.-Q. Yang, N. Zhang, M. Pagliaro, Y.-J. Xu, Chem. Soc. Rev. 43 (2014) 8240–8254.
- [7] S.J.A. Moniz, S.A. Shevlin, D.J. Martin, Z.-X. Guo, J.W. Tang, Energy Environ. Sci. 8 (2015) 731–759.
- [8] Z.L. Wang, Mater. Today 7 (2004) 26–33.
- [9] R. Boppella, K. Anjaneyulu, P. Basak, S.V. Manorama, J. Phys. Chem. C 117 (2013) 4597–4605.
- [10] A. McLaren, T.V.-S. G.Q. Li, S.C. Tsang, J. Am. Chem. Soc. 131 (2009) 12540–12541.
- [11] L.P. Xu, Y.-L. Hu, C. Pelligra, C.-H. Chen, L. Jin, H. Huang, S. Sithambaram, M. Aindow, R. Joesten, S.L. Suib, Chem. Mater. 21 (2009) 2875–2885.
- [12] Z. Chen, N. Zhang, Y.-J. Xu, CrystEngComm 15 (2013) 3022–3030.
- [13] Y. Liu, Z.H. Kang, Z.H. Chen, I. Shafiq, J.A. Zapien, I. Bello, W.J. Zhang, S.T. Lee, Cryst. Growth Des. 9 (2009) 3222–3227.
- [14] J.-F. Tang, H.-H. Su, Y.-M. Lu, S.-Y. Chu, CrystEngComm 17 (2015) 592–597.
- [15] L. Pan, T. Muhammad, L. Ma, Z.-F. Huang, S.B. Wang, L. Wang, J.-J. Zou, X.W. Zhang, Appl. Catal. B: Environ. 189 (2016) 181–191.
- [16] M.L. Huang, S.X. Weng, B. Wang, J. Hu, X.Z. Fu, P. Liu, J. Phys. Chem. C 118 (2014) 25434–25440.
- [17] E.S. Jang, J.-H. Won, S.-J. Hwang, J.-H. Choy, Adv. Mater. 18 (2006) 3309–3312.
- [18] S. Maiti, S. Pal, K.K. Chattopadhyay, CrystEngComm 17 (2015) 9264–9295.
- [19] Y. Chen, H. Zhao, B. Liu, H.Q. Yang, Appl. Catal. B: Environ. 163 (2015) 189–197.
- [20] B. Weng, M.-Q. Yang, N. Zhang, Y.-J. Xu, J. Mater. Chem. A 2 (2014) 9380–9389.
- [21] L.F. Wang, S.H. Liu, Z. Wang, Y.L. Zhou, Y. Qin, Z.L. Wang, ACS Nano 10 (2016) 2636–2643.
- [22] H.M. Chen, C.K. Chen, M.L. Tseng, P.C. Wu, C.M. Chang, L.-C. Cheng, H.W. Huang, T.S. Chan, D.-W. Huang, R.-S. Liu, D.P. Tsai, Small 9 (2013) 2926–2936.
- [23] N.S. Han, D. Kim, J.W. Lee, J. Kim, H.S. Shim, Y. Lee, D. Lee, J.K. Song, ACS Appl. Mater. Interfaces 8 (2016) 1067–1072.
- [24] C. Han, M.-Q. Yang, B. Weng, Y.-J. Xu, Phys. Chem. Chem. Phys. 16 (2014) 16891–16903.
- [25] Y.M. He, Y. Wang, L.H. Zhang, B.T. Teng, M.H. Fan, Appl. Catal. B: Environ. 168–169 (2015) 1–8.
- [26] D.M. Chen, K.W. Wang, D.G. Xiang, R.L. Zong, W.Q. Yao, Y.F. Zhu, Appl. Catal. B: Environ. 147 (2014) 554–561.
- [27] C. Eley, T. Li, F.L. Liao, S.M. Fairclough, J.M. Smith, G. Smith, S.C.E. Tsang, Angew. Chem. Int. Ed. 53 (2014) 7838–7842.
- [28] H. Zhang, R.L. Zong, Y.F. Zhu, J. Phys. Chem. C 113 (2009) 4605–4611.
- [29] J.S. Zhang, Y. Chen, X.C. Wang, Energy Environ. Sci. 8 (2015) 3092–3108.
- [30] A. Sinhamahapatra, J.-P. Jeon, J.-S. Yu, Energy Environ. Sci. 8 (2015) 3539–3544.
- [31] H. Song, Y.G. Li, Z.R. Lou, M. Xiao, L. Hu, Z.Z. Ye, L.P. Zhu, Appl. Catal. B: Environ. 166–167 (2015) 112–120.
- [32] D. Liu, Y.H. Lv, M. Zhang, Y.F. Liu, Y.Y. Zhu, R.L. Zong, Y.F. Zhu, J. Mater. Chem. A 2 (2014) 15377–15388.

- [33] Z. Jin, Y.-X. Zhang, F.-L. Meng, Y. Jia, T. Luo, X.-Y. Yu, J. Wang, J.-H. Liu, X.-J. Huang, *J. Hazard. Mater.* 276 (2014) 400–407.
- [34] Z.W. Wang, G.W. Meng, Z.L. Huang, Z.B. Li, Q.T. Zhou, *Nanoscale* 6 (2014) 15280–15285.
- [35] Z.Q. Cheng, M.Y. Yu, G.X. Yang, L.J. Kang, *CrystEngComm* 17 (2015) 1765–1768.
- [36] D.M. Chen, Z.H. Wang, T.Z. Ren, H. Ding, W.Q. Yao, R.L. Zong, Y.F. Zhu, *J. Phys. Chem. C* 118 (2014) 15300–15307.
- [37] A. Kar, S. Sain, D. Rossouw, B.R. Knappett, S.K. Pradhan, A.E.H. Wheatley, *Nanoscale* 8 (2016) 2727–2739.
- [38] S. Yamazaki, N. Nakamura, *J. Photochem. Photobiol. A: Chem.* 193 (2008) 65–71.
- [39] X. Jin, W.F. Sun, Z.H. Chen, T.-H. Wei, C.Y. Chen, X.D. He, Y.B. Yuan, Y. Li, Q.H. Li, *ACS Appl. Mater. Interfaces* 6 (2014) 8771–8781.
- [40] Q.H. Li, X. Jin, X.W. Yang, C.Y. Chen, Z.H. Chen, Y.C. Qin, T.-H. Wei, W.F. Sun, *Appl. Catal. B: Environmental* 162 (2015) 524–531.
- [41] D.D. Lin, H. Wu, R. Zhang, W. Pan, *Chem. Mater.* 21 (2009) 3479–3484.
- [42] S. Bai, X.Y. Li, Q. Kong, R. Long, C.M. Wang, J. Jiang, Y.J. Xiong, *Adv. Mater.* 27 (2015) 3444–3452.
- [43] Y.L. Lai, M. Meng, Y.F. Yu, *Appl. Catal. B: Environ.* 100 (2010) 491–501.
- [44] H.B. Fu, T.G. Xu, S.B. Zhu, Y.F. Zhu, *Environ. Sci. Technol.* 42 (2008) 8064–8069.